Applied Surface Science 632 (2023) 157601

Contents lists available at ScienceDirect

Applied Surface Science

journal homepage: www.elsevier.com/locate/apsusc

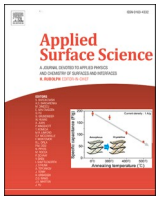

Full Length Article

Oxidation behaviour of uncoated and PDC-SiAlOC glass-coated TiAl at 750 °C in dry and humid air

Maciej Bik [a,*], Mathias Galetz [b], Lukas Mengis [b], Emma White [b], Wojciech Wieczorek [a], Klaudia Łyszczarz [a], Krzysztof Mroczka [c], Jakub Marchewka [a], Maciej Sitarz [a]

[a] AGH University of Science and Technology, Faculty of Materials Science and Ceramics, al. Mickiewicza 30, 30-059 Kraków, Poland
[b] DECHEMA-Forschungsinstitut, Theodor-Heuss-Allee 25, D-60486 Frankfurt am Main, Germany
[c] Cracow University of Technology, Faculty of Materials Engineering and Physics, Kraków, Poland

ARTICLE INFO

Keywords:
Polymer derived ceramics
SiAlOC glasses
48-2-2 TiAl alloy
Isothermal oxidation
Raman confocal imaging
EPMA

ABSTRACT

In this work polymer derived ceramic (PDC) coatings, based on SiAlOC glasses, were successfully applied on 48-2-2 TiAl alloy samples. These coatings showed a significant improvement in oxidation resistance in both dry and humid air conditions. The uncoated 48-2-2 TiAl alloy material showed poor oxidation resistance independent of the atmosphere. SEM, EPMA and Raman confocal imaging were used to investigate the oxidation mechanisms of the uncoated and coated 48-2-2 TiAl alloy in dry and humid air. The coating suppressed outward Ti diffusion and promoted alumina scale formation.

1. Introduction

TiAl alloys have emerged within the aviation industry as a possibility for replacing commonly used Ni-based superalloys. TiAl alloys offer a 2x lower density and can be used, for example, as low pressure turbine blades, affording lower fuel consumption and noise reduction as demonstrated in GEnx™ jet engines [1,2]. However, further development of these intermetallic alloys has been hindered by their unsatisfactory oxidation resistance above 700 °C [3,4]. Three approaches have been explored to overcome this issue: alloy development (towards 3rd and 4th generation TiAl alloys [5]), surface treatments (i.e. fluorine effect [6,7]), and diffusion layers [8–10] and other coatings [11]. Since the most recent works [10,12–15] still suggest a maximum working temperature of 700–750 °C for TiAl alloys, the demand for alternatives still persists.

Polymer derived ceramics (PDCs) are a unique, attractive group of materials due to their high thermomechanical stability, oxidation and chemical resistance. Being mainly silicon-based, PDCs also offer the possibility to modify the chemical composition in order to tailor the structure and desired properties [16]. Recently many works on PDCs for high temperatures have been published [17–20]. Among these, silicon oxycarbide (SiOC) glasses, sometimes called “black” glasses due to their color, are very interesting due to the possibility to tailor their properties, i.e. high oxidation resistance for a specific applications [21,22]. Considerable improvement in oxidation resistance was observed for SiOC-coated Crofer 22APU-based SOFC interconnects [23], and, more importantly, for SiOC-coated TiAl [24]. In the latter work, the high potential of using PDCs on TiAl alloys was demonstrated after 100 h of oxidation at 800 °C, but some shortcomings were still observed [24]. Despite the beneficial formation of Al_2O_3 and Z phase ($Ti_5Al_3O_2$), a very thin, continuous mixed Al_2O_3 + TiO_2 scale formed below the coating, which suggests that oxidation was not entirely suppressed [24]. The unsatisfactory results can be explained by the very small differences in the thermodynamic stability of TiO_2 and Al_2O_3, both more stable than SiO_2 [25]. By adding Al into a SiOC coating on TiAl the partial pressure below the coating should be significantly reduced.

Therefore, the main aim of this work was to increase the protective oxidation properties of SiOC-coated TiAl by increasing the Al content within the coating through application of an Al-doped SiOC (SiAlOC) glass. An improvement of the oxidation resistance of such a coating on ferritic steels has already been reported in humid environments [26] and for high temperature oxidation [27] where Al-doped material was much more resistant than pure SiOC.

TiAl alloys have been frequently studied in water vapor-containing atmospheres [28] because of their prevalence in various applications, i.e. for rotor materials in steam power plants [29], engine components of race cars [30,31], accident-tolerant fuel claddings in nuclear power plants [32], and turbocharger systems in exhaust gases [33]. Based on

* Corresponding author.
E-mail address: mbik@agh.edu.pl (M. Bik).

https://doi.org/10.1016/j.apsusc.2023.157601
Received 25 February 2023; Received in revised form 4 May 2023; Accepted 23 May 2023
Available online 27 May 2023

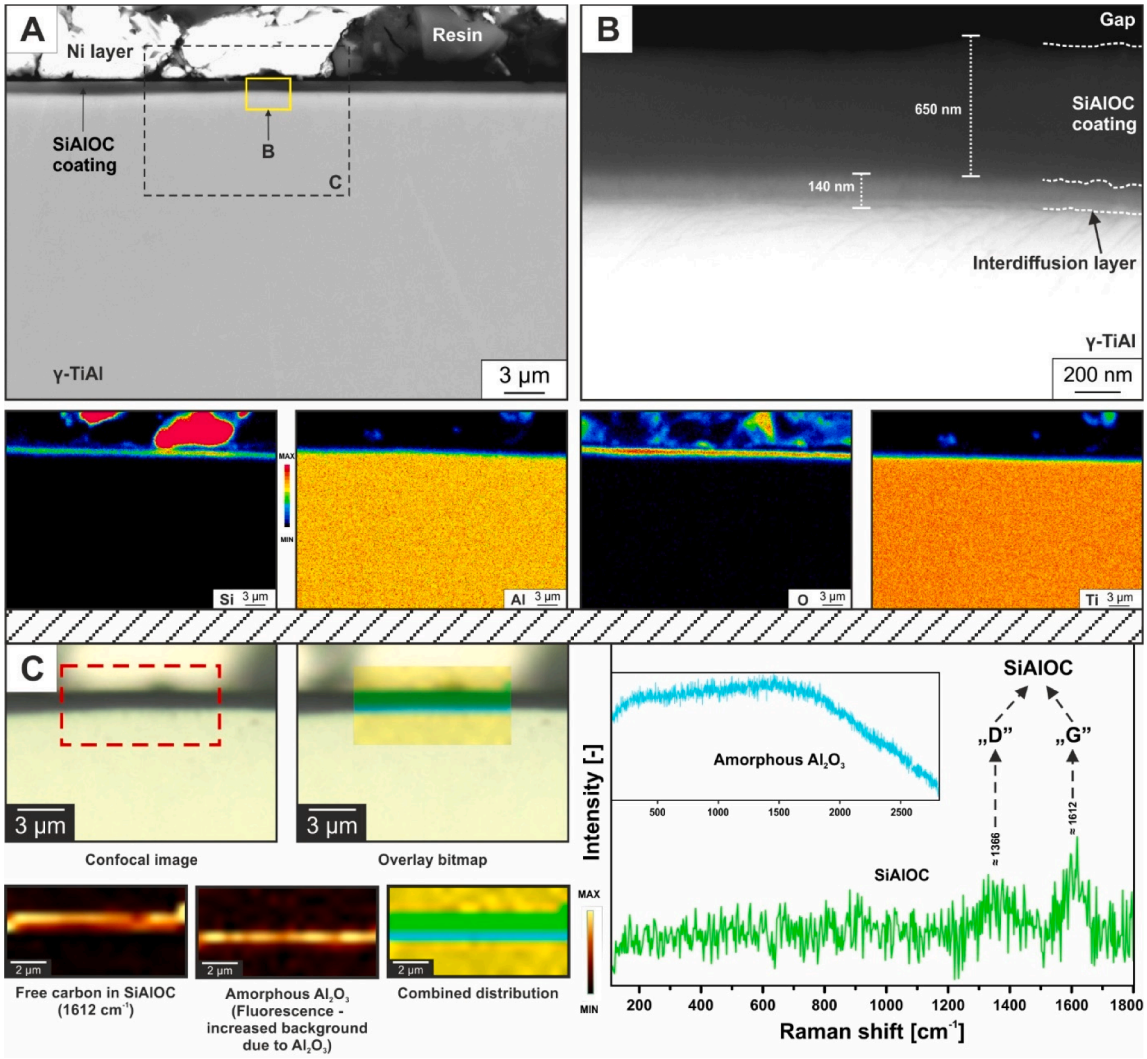

Fig. 1. Cross-sectional SEM images – A, B and EPMA analysis (area in Fig. A); C) Raman confocal imaging – for all Raman results the distribution images of the phases (based on integration of the characteristic band with the Raman shift given in the brackets) are presented with the corresponding spectra.

[34,35] water vapor significantly decreases the oxidation resistance of Ti and TiAl alloys. In [14,31] it was concluded that water vapor mainly enhances internal Al oxidation. Therefore, one additional aim of this work was to determine whether SiAlOC coatings improve TiAl alloy resistance to water vapor-containing atmospheres.

2. Experimental

2.1. Materials

Commercially used 48-2-2 TiAl alloy (Ti-48Al-2Cr-2at.%Nb, also known as "4822") ingots, were provided by GfE Metalle und Materialien GmbH, Nürnberg, Germany. Samples with dimensions of 20x20x3 mm were cut from the ingots using electro-discharge machining (EDM) and subsequently ground with SiC papers up to P800 grit. Prior to the coating deposition they were degreased in ethanol and acetone. The SiAlOC coating procedure (sol–gel synthesis, deposition with dip-coating technique, and two-step thermal treatment) has been previously described in detail in [26,27,36].

2.2. Methods

Both uncoated (also ground up to P800 grit) and SiAlOC-coated TiAl specimens were oxidized at 750 °C in both dry and humid (+10 vol% H_2O) air for 1000 h. For each condition, eight samples (four coated and four uncoated) were exposed and after 100, 300, 500 and 1000 h mass changes were recorded and one sample each was removed at each timestep. Subsequently, surface and cross-sectional microstructures were investigated.

The sample surfaces were examined with scanning electron microscopy (SEM) using a ThermoFischer Scientific Phenom XL Desktop unit (backscattered electron (BSE) mode, 10 kV accelerating voltage and high vacuum (<0.1 Pa)). Cross-sections of all specimens (including the as-coated state) were prepared by cutting the samples in half, depositing a very thin layer of Au (~40 nm) using a Leica EM ACE200 sputtering device, Ni-plating (~2–5 µm) using a Watts bath, hot embedding in conductive resin, and metallographic preparation by water grinding with SiC papers up to P2400 grit with subsequent polishing with diamond pastes down to 1 µm.

The microstructures of the cross-sections were investigated using a Schottky field emission scanning electron microscope (SU5000 Hitachi in BSE mode, high vacuum (1 Pa) and 20 kV accelerating voltage). The elemental compositions of the cross-sections were analyzed using electron probe microanalysis (EPMA) with a Jeol JXA-8100 instrument (W cathode and accelerating voltage of 15 kV for mapping).

Additionally, for select samples Raman spectroscopy with a WITec alpha 300 M+ spectrometer was used with 488 and 633 nm excitation wavelengths with laser spots of ca. 650 nm and 850 nm in diameter,

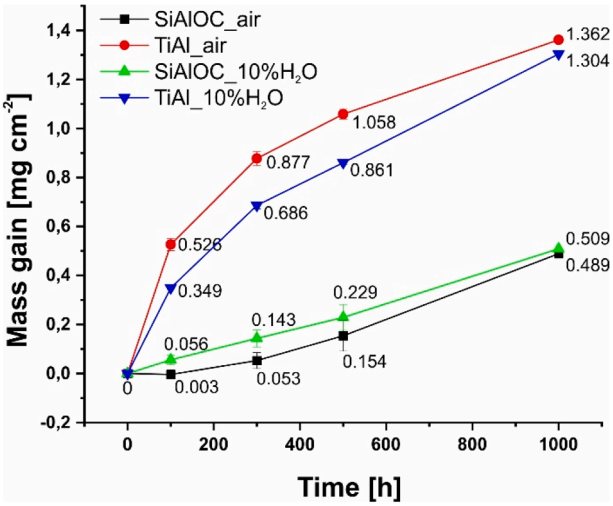

Fig. 2. Oxidation kinetics of both uncoated and SiAlOC-coated 48-2-2 TiAl alloy in dry and humid air.

respectively. The laser power was adjusted by the oscilloscope mode to prevent sample degradation/phase transformation, and a 100x ZEISS Epiplan-Neufluar objective with NA = 0.9, 600 grooves/mm grating and Andor CCD detector was used. The scanning area during mapping was always 10 μm in width and from 5 to 20 μm in height, depending on the scale thickness. Single accumulations lasted 2 s and the sampling density was 500 nm. WITec Control FIVE, as well as WITec Project FIVE 5.3 PLUS and OPUS 7.2 softwares were used to collect and post-process the Raman data, respectively. The post-processing procedure included the following steps: extracting the desired range (110 – 1800 cm^{-1}), removing cosmic spikes (the CRR filter), and spectra integration (using a special filter of predefined width and position depending on the analyzed phase, e.g. the 555 cm^{-1} band for Cr_2O_3). As a result, Raman distribution images in the form of component/chemical concentration maps, as well as the most representative spectra for each phase, were extracted manually. Such spectra were then subjected to a baseline correction process using a polynomial function and the distribution images were put together to form a combined distribution image that was subsequently overlayed with a previously taken confocal image of the investigated area. According to these combined distribution maps, the predominant phase can be identified in each region; however, this does not exclude other phases from also being present in the same areas.

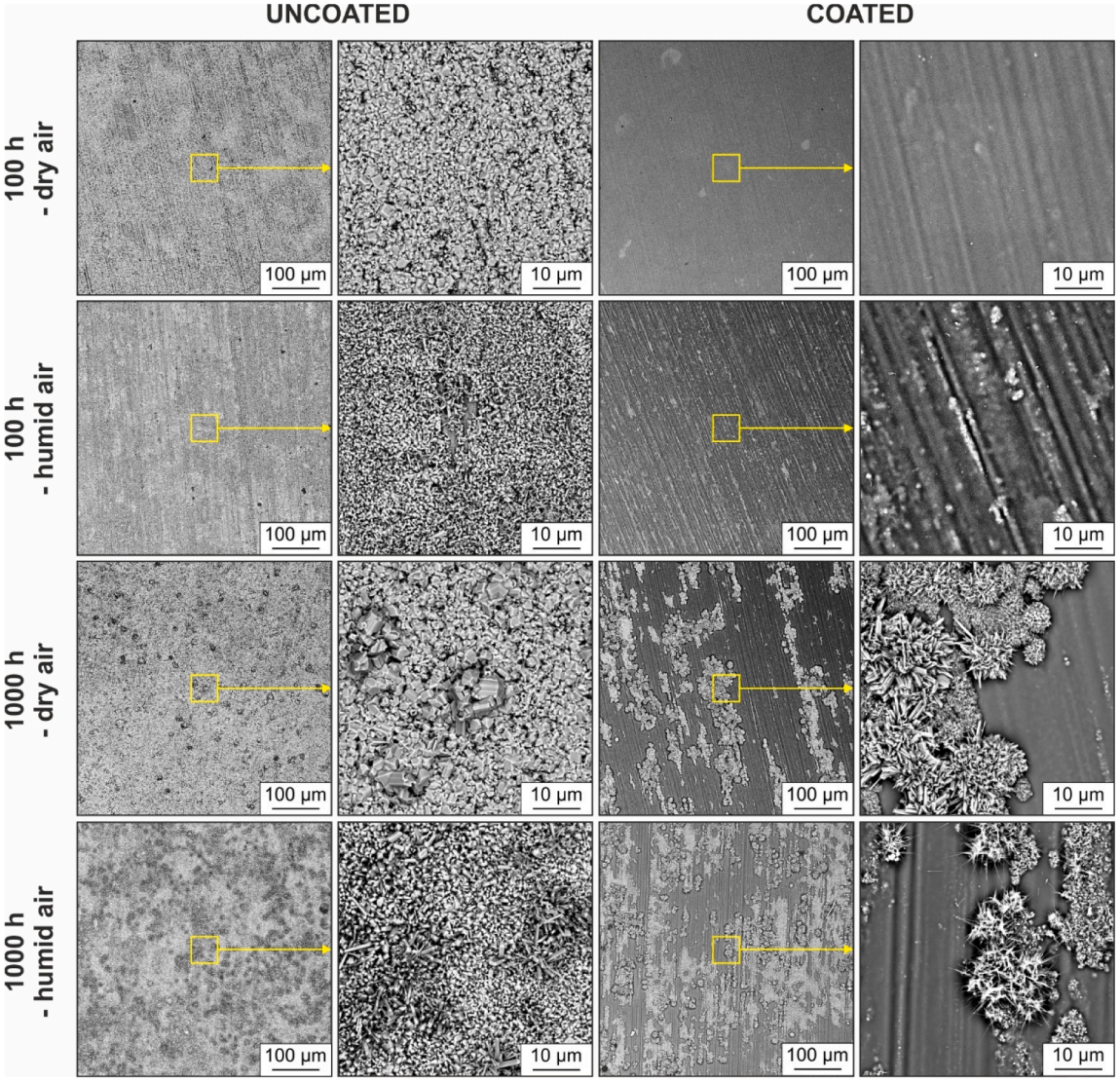

Fig. 3. Surface microstructures of both uncoated and SiAlOC-coated 48-2-2 TiAl alloy oxidized in dry and humid air.

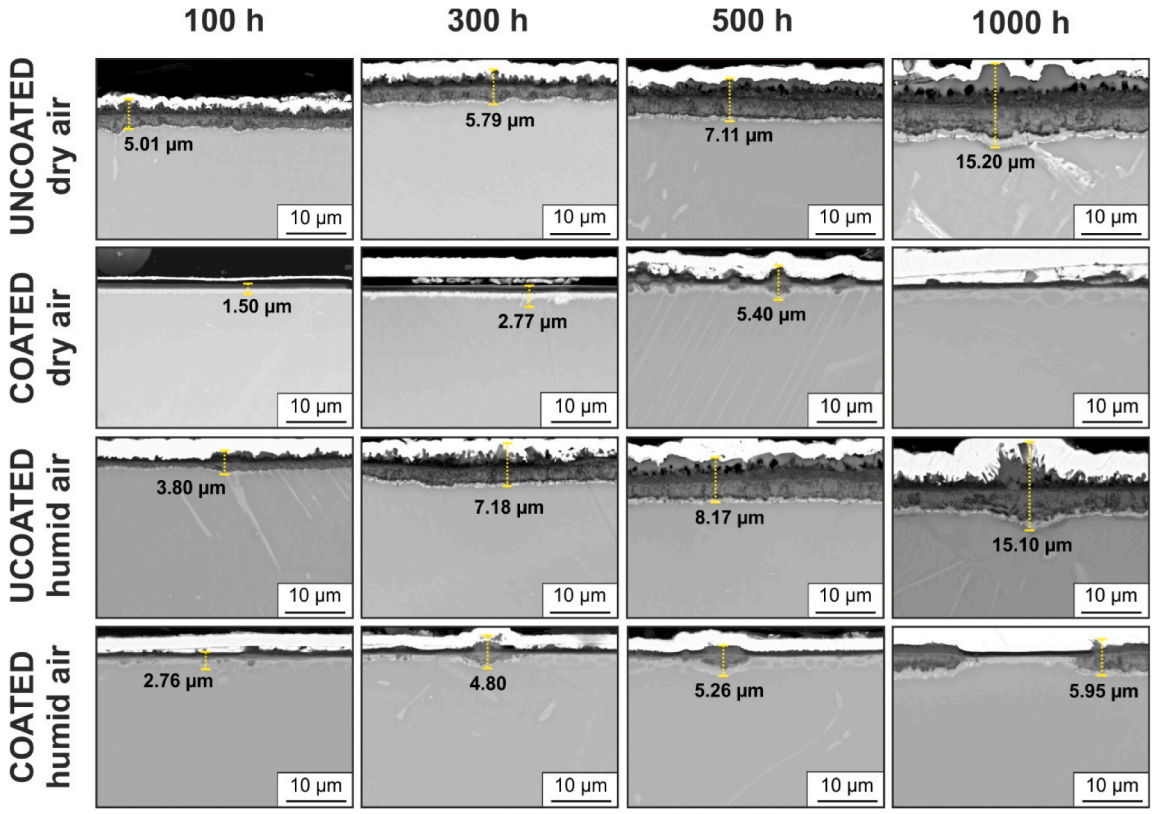

Fig. 4. Cross-sectional microstructures of both uncoated and SiAlOC-coated 48-2-2 TiAl alloy oxidized in dry and humid air.

3. Results

3.1. Coating structure

Pyrolysis of the dip-coated TiAl specimens resulted in the formation of continuous, ca. 650 nm SiAlOC glass coatings that were chemically bonded to the substrate material (See Fig. 1A and B). Underneath was a thin interdiffusion/reaction zone of around 140 nm in thickness. EPMA maps confirmed that the obtained coating was composed of Si, Al and O (the C-map was not included due to the interfering signal of the mounting resin). Raman confocal imaging of the outer coating confirmed "free carbon" within the SiAlOC glass coating [26,37], which was detected using a 488 nm laser line based on the presence of bands at ca. 1366 and 1612 cm^{-1}. The inner coating was also investigated using a 633 nm excitation wavelength due to the presence of a higher background that can be attributed to amorphous alumina [38]. However, in the case of Al_2O_3 it is highly possible that the signal was distorted due to the very low thickness of the interdiffusion layers, below the lateral resolution of Raman imaging with a 633 nm line (~430 nm).

3.2. Oxidation kinetics

In Fig. 2 the mass changes after dry and humid air exposures of the coated and uncoated TiAl are shown. During the 1000 h of exposure no significant influence of the added water vapor was observed for both the coated and uncoated samples. At shorter oxidation times some slight variations can be observed for the uncoated alloy, with a trend of a slightly faster mass gain in dry air compared to humid air.

For the coated samples the influence of the humid air was also very minimal, but the specific mass gain was much lower for both conditions when compared with the uncoated material. After 1000 h the mass gain was ~ 2.5 times lower for the coated TiAl.

3.3. Surface and cross-sectional microstructures

SEM surface images of the exposed samples are shown in Fig. 3. After only 100 h the uncoated material is covered with a distinctly different oxide morphology for dry versus humid air. This difference becomes more pronounced when looking at the samples exposed for up to 1000 h. In dry air larger hexagonal prisms were observed on top of smaller ones; whereas, in humid air the scale morphology changes to mostly columnar and needle-like crystals. For the coated specimens after 100 h, no oxide crystals were observed in dry air, while initial oxide crystals were present after humid air exposure. For longer oxidation times, both samples showed oxide crystals with some variations between the dry and humid air conditions. For dry oxidation most of the scale was composed of small-sized crystals interrupted by coarser ones with a needle-like morphology. For humid oxidation larger areas of these whisker/acicular oxides were found, which in both cases seemed to nucleate along grinding grooves.

The subsurface zone below the oxide scale is equally important for TiAl alloys, which often show oxygen uptake and nitridation. In Fig. 4 the cross-sectional microstructures of all samples are given. After 100 h of oxidation, the uncoated alloy showed a multicomponent scale that was slightly thicker for dry air exposure. After 1000 h the scale thicknesses increased to about 15 µm in the thickest spots for both dry and humid air. In the cross-sections the hexagonal grains and needles for dry and humid air are again visible and correspond well to the SEM surface observations from Fig. 3. For the coated alloys the near surface zone after 100 h showed the first signs of internal oxidation under the coating for humid air conditions. After 1000 h in both dry and humid air, localized internal oxidation and breakaway was observed. For dry air this breakaway manifested in oxide outward growth above the coating residues, while in humid air the oxide formed primarily by inward growth.

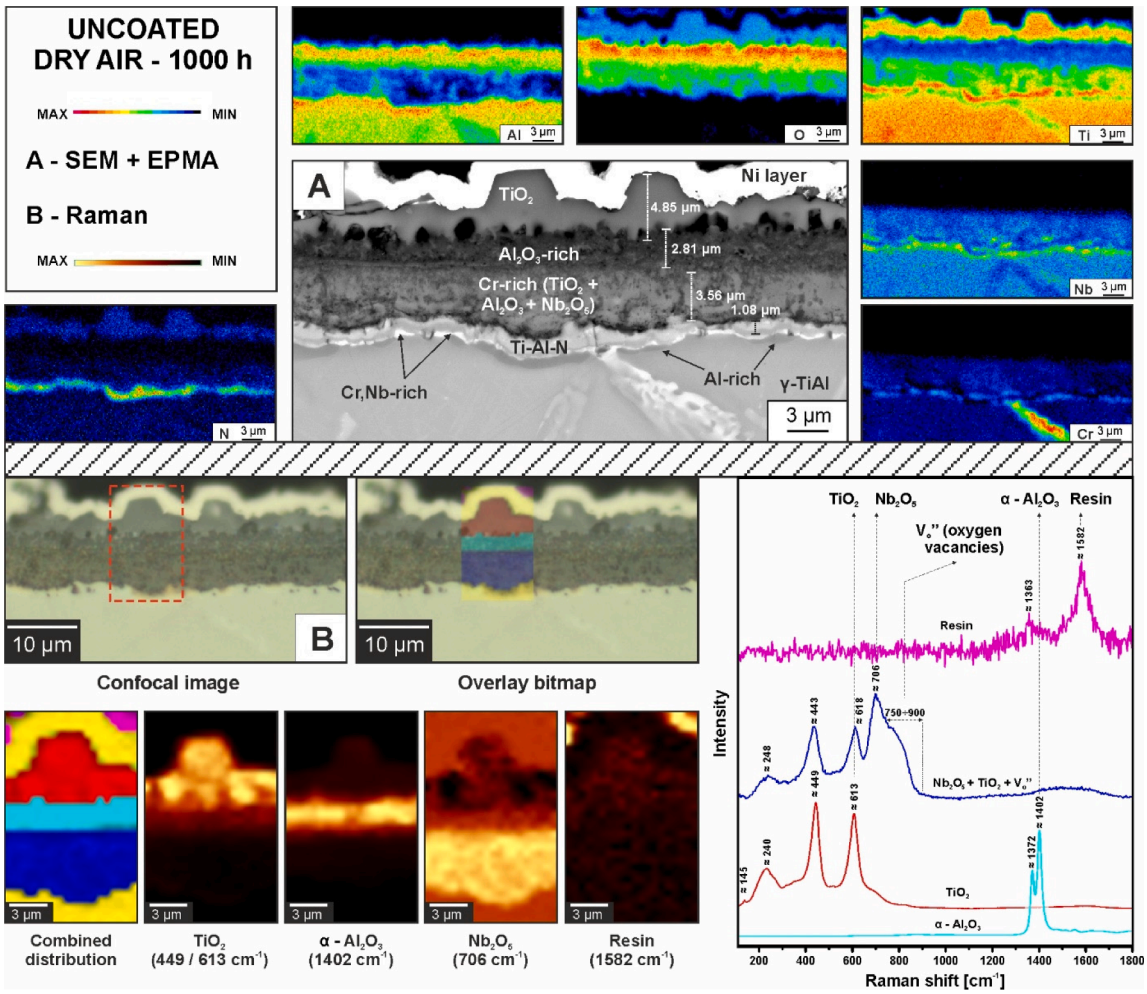

Fig. 5. A) Cross-sectional microstructure and EPMA analyses, and B) Raman imaging (confocal image corresponds to the same area in Fig. A) of uncoated 48-2-2 TiAl alloy oxidized for 1000 h in dry air conditions.

3.4. Phase and elemental analysis

3.4.1. Uncoated alloy

In order to further characterize these multilayered and multicomponent systems, EPMA elemental analysis and Raman spectroscopy phase analysis were carried out after 1000 h for the uncoated substrates and after 300 h and 1000 h exposure for the coated alloy. Fig. 5A and B illustrate a typical cross-sectional microstructure of the uncoated 48–2-2 alloy after 1000 h in dry air. Based on EPMA analysis (Fig. 5 – top) and Raman spectroscopy (Fig. 5 – bottom), the observed scale is composed of external hexagonal TiO_2, an inner Al_2O_3–rich layer, and a porous, Cr-rich mixture of alumina and titania at the alloy interface. Additionally, Raman imaging revealed an underlying mixed oxide region of rutile TiO_2 (449 and 613 cm^{-1} bands) + Al_2O_3 (1402 cm^{-1} mode) and a considerable amount of Nb_2O_5, based on the high intensity of the band at ca. 705 cm^{-1}. The EPMA map for Cr shows an increased concentration below the nitride layer suggesting the presence of a Laves phase, which was found before to emerge from an oxygen-driven $\beta \rightarrow \alpha 2 + \gamma +$ Laves decomposition during oxidation [13]. Finally needle-like changes in the microstructure can be seen for this uncoated alloy, which is an indication of oxygen uptake. For the uncoated material no significant differences are apparent when comparing the humid versus dry air exposures (comparing Figures 5 and S1 (Supplementary Materials)) apart from the morphology of the outer TiO_2 scale, as described earlier.

3.4.2. Coated alloy in dry air

For the coated alloy oxidized in dry air, the 300 and 1000 h results are shown in Figs. 6 and 7, respectively. Fig. 6 presents the coated alloy after 300 h with a ~ 290 nm thick interdiffusion layer (Fig. 6B). Al is depleted below the coating and no nitridation is observed. Further microstructural changes can be seen in the elemental contrast (BSE mode) in Fig. 6B, which are below the resolution limit of the EPMA, such as a roughly 450 nm thick outward diffusion layer in the oxide scale of the region marked as “Beginnings of breakaway”. Fig. 6C illustrates the confocal optical image of exactly the same region depicted in Fig. 6B but examined with Raman spectroscopy. With Raman it can be observed that the SiAlOC coating still contains free carbon that was not released/oxidized based on the 1354 and 1599 cm^{-1} bands [21,37]. Moreover, measurements with the 633 nm laser line show the typical bands at ca. 1372 and 1402 cm^{-1} [39,40] meaning α-Al_2O_3 is the main component of these regions, which explains the Al depletion underneath. Additionally, the nucleation of rutile TiO_2 was observed as proven by the occurrence of the Raman modes at around 452 and 602 cm^{-1} [41,42]. Their low signal-to-noise ratio indicates a very early stage of TiO_2 formation. Below the oxide scale Cr enriched precipitates were evident, suggesting again the presence of a Laves phase as already observed for the uncoated alloys [12].

After 1000 h the breakaway degradation area was much more pronounced (Fig. 7A and B), but there were still regions where the coating remained protective (Fig. 7C and D). Fig. 7C shows a large area without breakaway degradation. Fig. 7D shows a magnified, representative

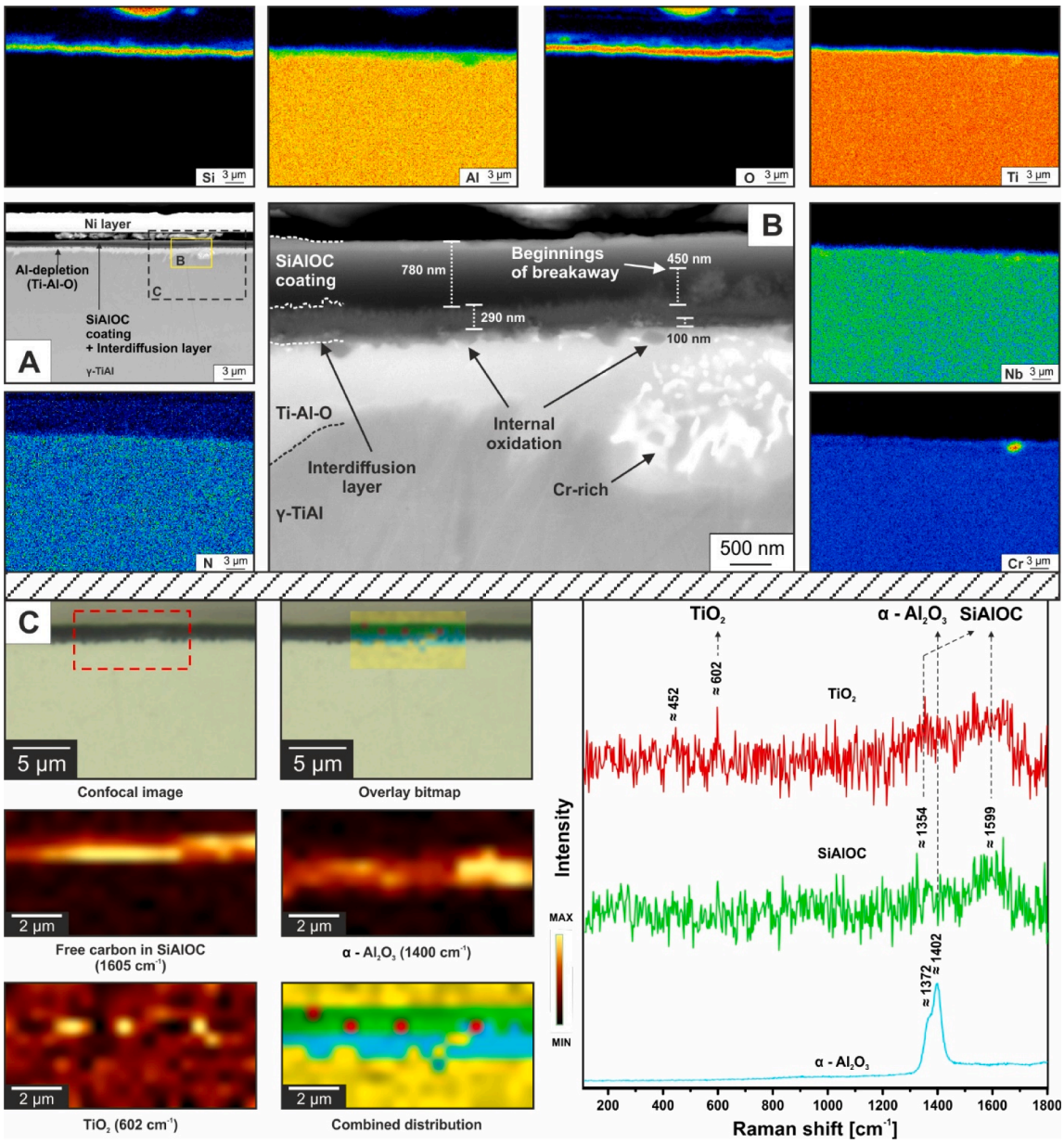

Fig. 6. A) and B) Cross-sectional microstructure and EPMA analysis (area in Fig. A); C) Raman confocal imaging of SiAlOC-coated 4822 TiAl alloy oxidized for 300 h in dry air conditions.

region of this protected region after 1000 h in dry air. The Al depletion zone, in which an increase in oxygen can be measured, grew further when compared to 300 h (Fig. 6B). EPMA maps of Ti and Al suggest that it is a strongly Al-denuded zone labeled as "Ti-Al-O", which according to literature can be either O-rich α_2-Ti_3Al and/or Z-phase according to [31,43]. In addition, no N was detected, nor were there signs of Cr-rich precipitates in the microstructure below the scale. In the "breakaway" case EPMA analysis (Fig. 7 – top) revealed the presence of a continuous Si-rich layer, suggesting that the SiAlOC coating is still present after 1000 h of oxidation but failed locally and was then overgrown. Compared to the uncoated sample (Fig. 5) the separation of TiO_2 (on the surface) and Al_2O_3 within the scale is less pronounced based on Raman imaging (Fig. 7E). Using this technique again the formation of Nb_2O_5 within the inner part of the scale/breakaway area was confirmed, but no free carbon remained after 1000 h, which suggests C release from the SiAlOC layer during further oxidation. Moreover, in the regions with breakaway and failure of the coating, the internally affected zone is still thinner than for the uncoated substrate. Hence, even in failed regions there is a positive effect of the coating.

3.4.3. *Coated alloy in humid air*

When humid air exposures are compared to the dry air conditions, after 300 h (Fig. 8A and B) and 1000 h (Fig. 9) the thicknesses of the interdiffusion layers are similar and again no N uptake or internal oxides were detected in the protected regions. Just as in dry air (Fig. 6C) in humid air after 300 h (Fig. 8C), the free carbon Raman modes ca. 1360 and 1610 cm^{-1} were still detectable. In breakaway areas (Fig. 8B) the oxide scale was composed of Al_2O_3, as evidenced by the EPMA maps of Al and O and the Raman modes ca. 1370 and 1398 cm^{-1}, and of TiO_2, from the EPMA maps of Ti and O and the Raman modes ca. 242, 448 and 613 cm^{-1}. The elemental and phase analyses indicated Al_2O_3 and TiO_2 in the outer scale and Al_2O_3 with needle-like structures at the interface to the metal. The presence of Nb_2O_5 was confirmed by the EPMA map of Nb and the Raman mode ca. 702 cm^{-1} [44,45]. Oxygen vacancies (Raman modes within the 750–850 cm^{-1} region [46]) were also confirmed within the inner part of the scale as were traces of TiO_2 within

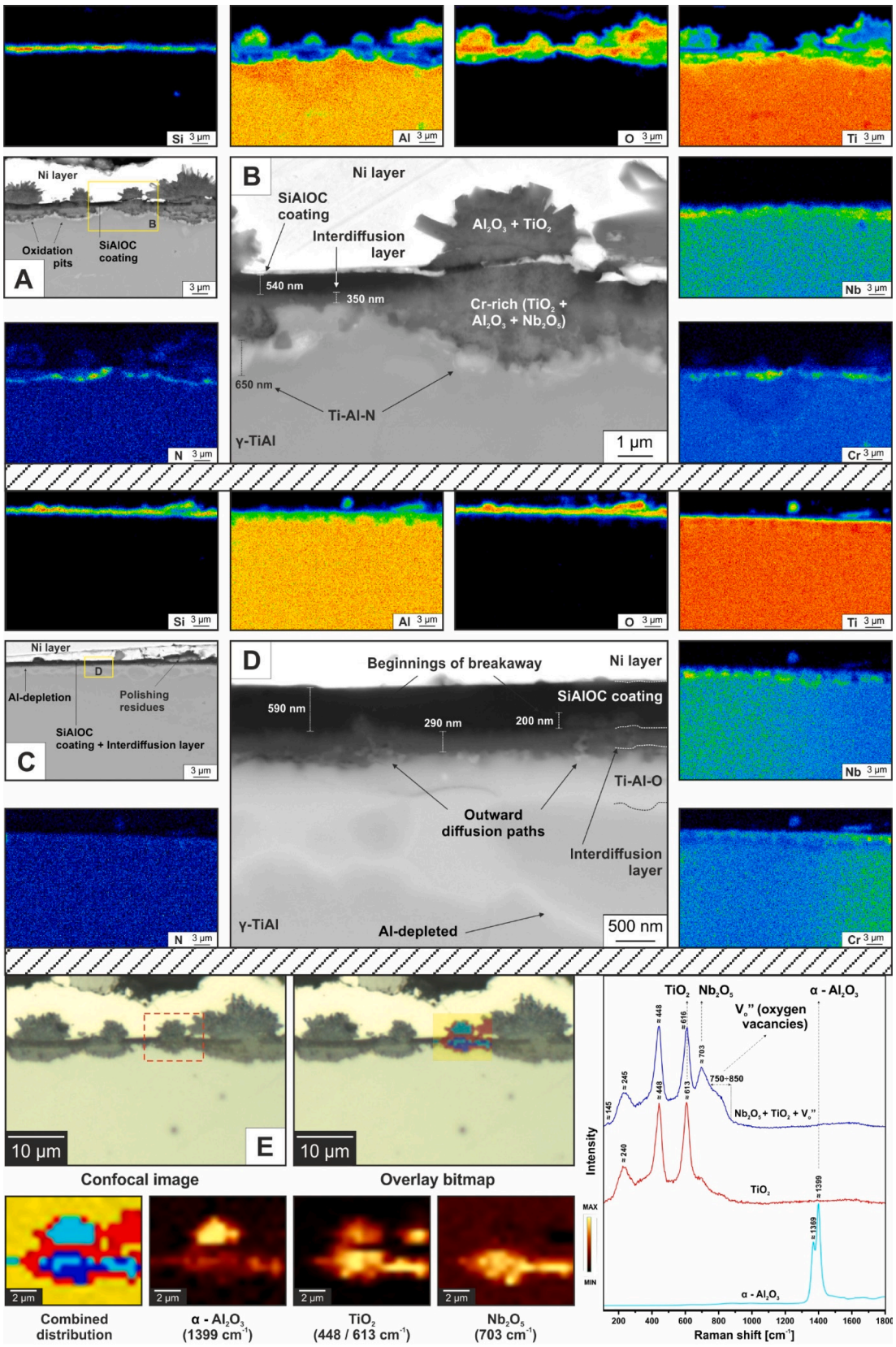

Fig. 7. Cross-sectional microstructures and EPMA analyses of SiAlOC-coated 48–2-2 TiAl alloy oxidized for 1000 h in dry air conditions: A) and B) Breakaway area; C) and D) Intact zone (the EPMA maps were taken from the boxed regions in Figs. A and C, respectively); E) Raman confocal imaging of the same area depicted in Fig. A.

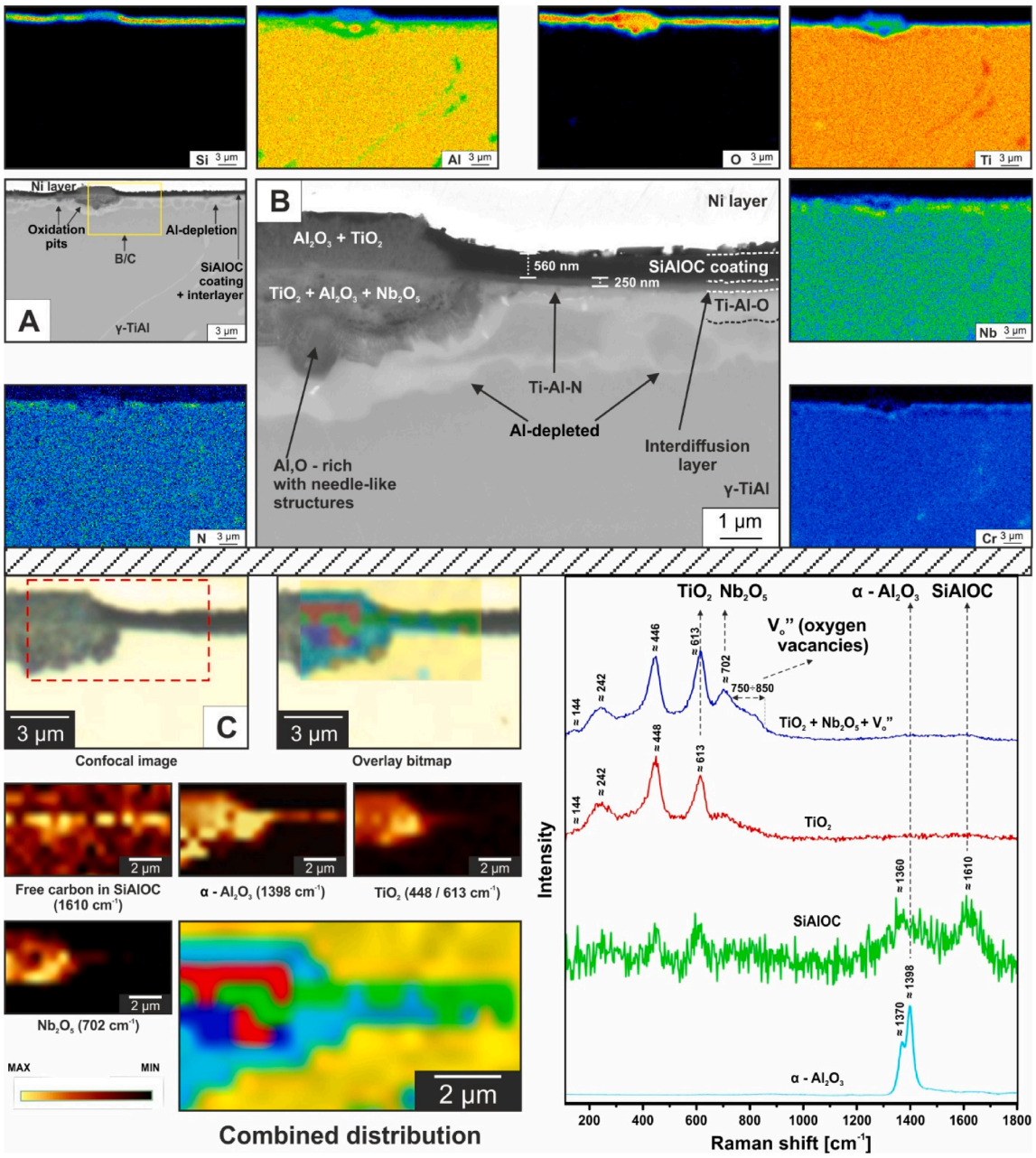

Fig. 8. A) and B) Cross-sectional microstructure and EPMA analysis (taken from Fig. A); C) Raman confocal imaging of SiAlOC-coated 48-2-2 TiAl alloy oxidized for 300 h in humid air conditions.

the SiAlOC coating.

For the breakaway areas after 1000 h, the scale consisted again of $Al_2O_3 + TiO_2$ (Fig. 9A and B). Below the breakaway areas N uptake was observed, as well as a continuous, Al-depleted Ti- and O-rich diffusion zone that also showed Nb- and Cr-rich regions. Fig. 9C shows that in breakaway regions a Cr-rich mixed oxide with TiO_2 and Nb_2O_5 with oxygen vacancies (ca. 238, 448 and 614 cm^{-1} – rutile TiO_2, 750–900 cm^{-1} – oxygen vacancies, and 702 cm^{-1} – Nb_2O_5) was formed. The combination of EPMA indicating an increased concentration of Al and Raman imaging with a high intensity at ca. 1400 cm^{-1} from the same area also confirmed the presence of Al_2O_3 (marked in Fig. 9B). One of the few distinct differences for oxidation under humid versus dry air was the internal oxidation of Al below the interdiffusion layer (Fig. 9A BSE image and Al EPMA map). Internal oxidation of Al has been previously observed for TiAl alloys oxidized in humid air [14,29].

Of all the samples that were investigated the humid air 1000 h specimen was the only one for which Raman imaging (Fig. 9C) confirmed the occurrence of a nitride layer based on the two broad regions within the 140–390 and 500–650 cm^{-1} spectral ranges resulting from TiAlN and or TiN, respectively [47,48]. According to [47] the higher intensity at ca. 250 cm^{-1} in the first region, as well as at around 610 cm^{-1} in the second one, implies a higher proportion of TiAlN over TiN within the nitride layer. Literature confirms weak Raman scattering of TiN and TiAlN [47,48] in contrast to very strong scattering for TiO_2 (using 488 line) and Al_2O_3 (using 633 nm line). Thus, it cannot be ruled out that smaller amounts of nitride were present in the other samples but remained undetected due to signal distortion by the other phases in the vicinity (especially TiO_2) or a too weak signal.

4. Discussion

In this study the oxidation results for a 48–2-2 TiAl alloy after dry

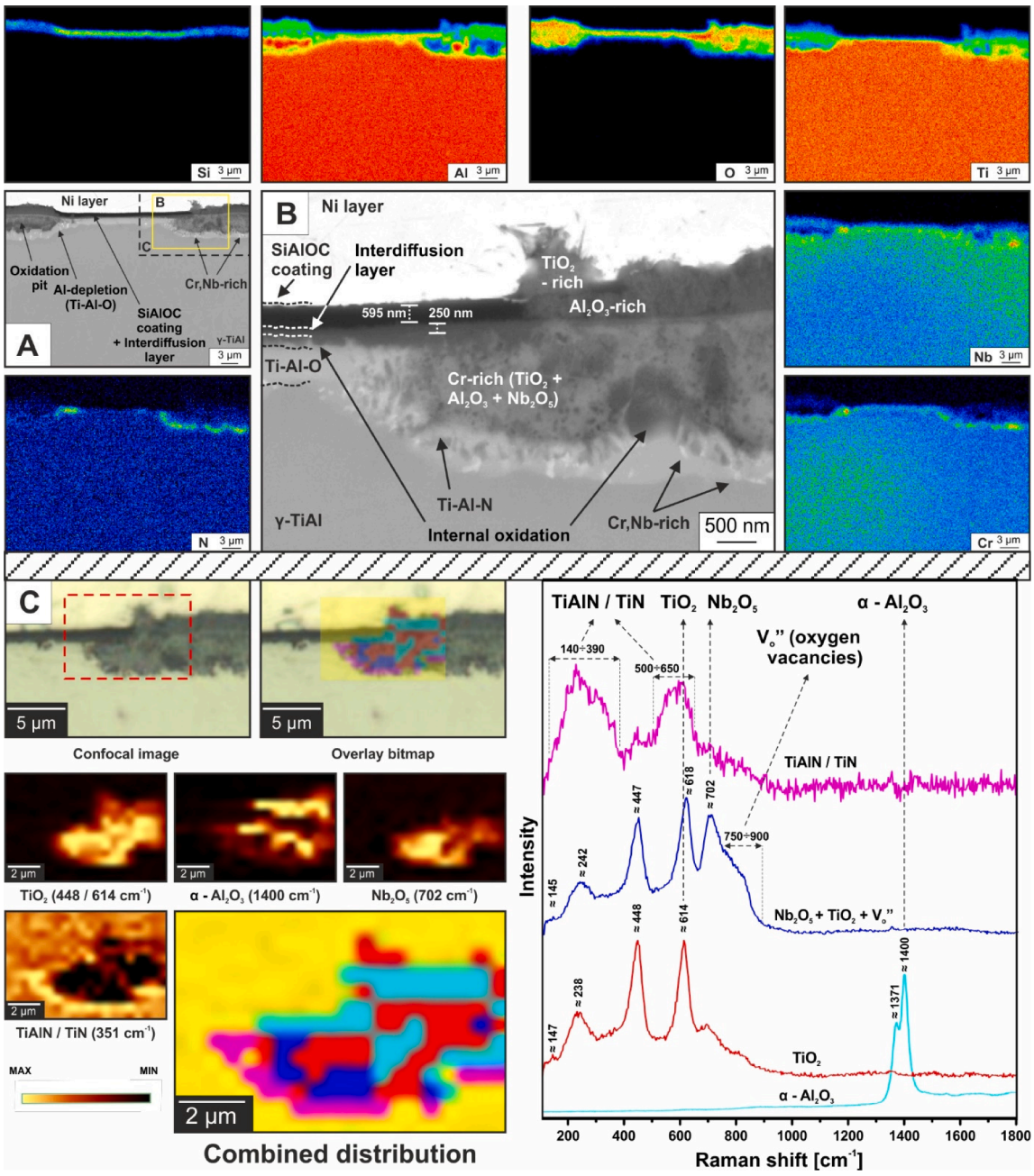

Fig. 9. A) and B) Cross-sectional microstructure and EPMA analysis (taken from Fig. A); C) Raman confocal imaging of SiAlOC-coated 48-2-2 TiAl alloy oxidized for 1000 h in humid air conditions.

and humid air exposures were very similar and no clear trend nor accelerated kinetics were observed, which is in contrast to what has been reported in other research. Several studies can be found for other TiAl alloys and temperatures where the presence of water vapor leads to a higher mass gain and thicker oxide scales when compared to samples treated in dry air [14,29,34]. In the present case, the most pronounced difference was the surface oxide morphology. In dry air an external hexagonal TiO_2 and inner Al_2O_3–rich layer was present which is typical for this alloy sublattice [41,42]. While hexagonal crystals appeared under dry air, needle-like crystals formed after humid air exposure which confirms the preferential growth of TiO_2. This observation is in line with other studies of TiAl alloys in humid air [14], as well as for Ti- and Ti-based alloys [35].

In the inner scale Raman spectroscopy revealed the presence of Nb_2O_5 in the lower portion of the mixed oxide scale after dry air exposure. These findings are in contrast to most literature where Nb is suggested to be only a constituent of Nb/Cr–rich regions (also marked in Fig. 5) and the cations (Nb^{5+}) are believed to substitute Ti^{4+} in the TiO_2 sublattice [49,50]. The broad shoulder within the 750–900 cm^{-1} range may originate from the oxygen vacancies that are well-known to exist within TiO_2 and also known to accelerate diffusion processes [25].

Below the main oxide scale nitridation was noticeable after dry air exposure for 300 and 1000 h, typically as Ti-Al-N and/or Ti-N [44]. Additionally, Al-rich regions, most likely $TiAl_2$ as seen in [13] or metastable mixed titanium–aluminum oxide phases such as Z-phase, could form at the interface [45].

When the TiAl alloy had been coated with SiAlOC a significant improvement in oxidation kinetics was achieved in dry air as well as humid conditions, and, similar to the uncoated results, the presence of water vapor did not accelerate oxidation. After 1000 h of oxidation, the

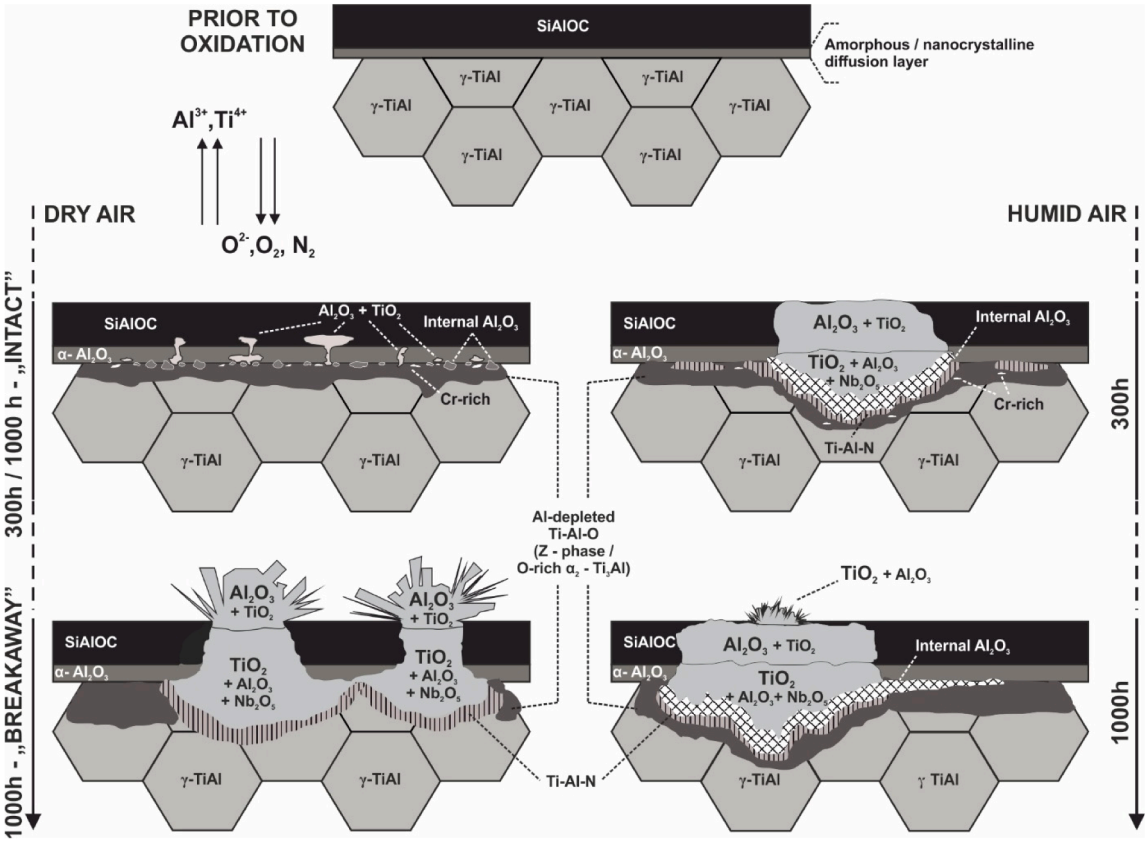

Fig. 10. Overview of degradation for SiAlOC coated 48-2-2 TiAl alloy oxidized in both dry and humid air conditions.

coated specimens exhibited a mass gain of around 0.5 mg/cm^2, and therefore, these SiAlOC-based PDCs can be classified as an efficient protection system for TiAl alloys [11]. Moreover, when comparing the obtained mass gains in dry air with other published coatings oxidized at the same temperature, SiAlOC protects TiAl alloy more efficiently. For example, NiCoCrAlY on Ti46.5Al1.5V1Cr0.2at.%Nb gained ca. 1 mg/cm^2 after 100 h, much higher than the 0.003 mg/cm^2 of the present study [51]. Also TiAlCr-Y on Ti45Al8at.%Nb showed a gain of ca. 0.2 mg/cm^2 after 500 h [52], again higher than the 0.154 mg/cm^2 observed for the SiAlOC coating. A very similar concept of a PDC amorphous layer based on SiBCN with an Si interlayer was used for oxidation protection of the same TiAl alloy (48-2-2) but was tested at 800 °C [53]. In this instance the mass gain for SiAlOC was only 0.489 mg/cm^{2}versus 0.59 mg/cm^2 for SiBCN after 1000 h, but the 50 °C higher testing temperature does need to be considered. Another difference is the mass vs. time dependance when comparing these two coatings. For the SiBCN-coated alloy, the behavior can be described using a parabolic law of oxidation similar to the uncoated 48-2-2 TiAl alloy [53]. For the SiBCN coating a reaction/interdiffusion layer based on $Ti_xSi_y(Al)$ formed that increased in thickness during oxidation [53]. Interestingly, SiAlOC-coated specimens exhibited linear-like oxidation behavior with slow kinetics, independent of the atmosphere humidity. For the SiAlOC coating a similar phenomenon was observed with a reaction/interdiffusion layer based on α-Al_2O_3 which would seem to indicate parabolic behavior. However, microcracks in the SiAlOC coating (Fig. 4) are a possible explanation of the observed linear kinetics.

In Fig. 10 an overview of the oxide formation and degradation mechanisms of the coating are shown. One main benefit of the coating is that a thin and continuous Al_2O_3 layer forms underneath, which proves that the PDCs lowered the oxygen partial pressure at the coating/alloy interface, and thus, promoted selective Al oxidation. This beneficial influence of the coating is also proven by the absence of hexagonal TiO_2 above the coating, showing that the Ti outward diffusion process was hindered. As can be seen in Fig. 1, the initial Al_2O_3 layer was already formed during the pyrolysis process in argon. Due to the higher thermodynamic stability of aluminum oxide, it can also react with oxygen from the coating. Oxidation in both atmospheres resulted in thickening of the initial amorphous alumina layer and subsequent crystallization to stable α-Al_2O_3. Comparing the scale morphology with the mixed TiO_2 + Al_2O_3 on PDC-SiOC coated TiAl alloy oxidized at 800 °C [24], it is suggested that the Al addition in the SiOC coating significantly suppressed TiO_2 formation.

After longer exposure times breakaway regions with multilayered oxide nodules were found locally on the coated alloy, similar to the uncoated alloy and characterized by outward Ti diffusion (marked as "Al_2O_3 + TiO_2" in Fig. 10). Below the breakaway areas N uptake was observed, as well as a continuous, Al-depleted Ti- and O-rich diffusion zone that also shows Nb- and Cr-rich regions. This Nb and Cr enrichment is much more pronounced in the vicinity of the breakaway areas, whereas only Nb enrichment can be seen where the coating is still intact. These results support the strong influence of Nb and Cr on the oxidation resistance of TiAl, which is discussed in [54]. The coating considerably suppressed the rate of oxidation in the areas where the coating was still intact, since such regions of breakaway occurred only locally and the microstructure looks very similar after 300 h and 1000 h (Fig. 10). The localized coating failure is potentially triggered through crack formation in the coating, possibly due to residual thermal stresses resulting from the thermal treatment prior to oxidation. Under the coating in the reaction zone, peculiar regions of distinct BSE contrast (Fig. 6B and 7D) are visible which suggest outward diffusion of cations heavier than Al^{3+} (supposedly Ti^{4+}) and then could be the sites of scale failure. In addition, the nucleation of localized titanium oxide inside the coating can be observed above these paths which also could be the initiation site for breakaway oxidation.

When the SiAlOC-coated TiAl alloy was oxidized in humid air only two differences were observed: 1) more pronounced internal oxidation,

as is typical for TiAl alloys oxidized in humid air [14,29], and 2) a change in the oxide scale morphology. In humid air the oxide scale grew in a more lateral direction, consuming the base material, and the outer part of the scale was dominated by Al_2O_3. This more lateral growth suggests a stronger influence of oxygen inward diffusion and slower Ti outward diffusion. Even though the oxide scales looked different depending on the atmosphere, the atmosphere had no appreciable influence on the overall mass gain (Fig. 2). In [29] it was reported that water vapor enhances oxygen uptake, which promoted internal oxidation of Al in a TNM alloy. According to [14] water vapor can dissociate into H^+ and OH^- ions that may dissolve in oxide scales and such hydroxyl anions diffuse faster [55] when compared to O^{2-}. In this work the involvement of Cr and Nb in the oxidation process was observed and might be the key to the lower impact of water vapor for this alloy when compared to the studies found in the literature. For the SiAlOC-coated alloy enhanced internal Al oxidation in humid air could also be explained by the accelerated hydroxyl anion diffusion. For ferritic steels SiAlOC coatings suppress outward cation diffusion significantly [27]. This agrees with the Ti ion outward diffusion observed within this study and explains the protective behavior of this coating. In future work, the local failure of the SiAlOC coating should be addressed and could be improved by altering the coating composition or the thermal treatment parameters (i.e. slower cooling for reduced residual stresses).

5. Conclusions

The most findings of this work are:

(a) In dry and humid air conditions no significant difference in oxidation kinetics was observed for the uncoated 48-2-2 alloy. The main difference between the two atmosphere exposures was the oxide scale morphology, with a preferential growth of TiO_2 in a whisker/needle-like manner in humid air.
(b) In both dry and humid conditions the oxidation resistance of the 48-2-2 alloy was significantly improved by the application of a SiAlOC coating.
(c) The SiAlOC coating on a 48-2-2 alloy formed a multilayered system with an Al-rich interdiffusion/reaction layer below the coating, which subsequently formed a continuous Al_2O_3 layer after oxidation at 750 °C.

CRediT authorship contribution statement

Maciej Bik: Conceptualization, Data curation, Funding acquisition, Investigation, Project administration, Resources, Visualization, Writing – original draft. **Mathias Galetz:** Conceptualization, Resources, Validation, Writing – review & editing. **Lukas Mengis:** Conceptualization, Investigation, Writing – review & editing. **Emma White:** Writing – review & editing. **Wojciech Wieczorek:** Investigation. **Klaudia Łyszczarz:** Investigation. **Krzysztof Mroczka:** Investigation. **Jakub Marchewka:** Investigation. **Maciej Sitarz:** Conceptualization, Resources, Validation.

Declaration of Competing Interest

The authors declare that they have no known competing financial interests or personal relationships that could have appeared to influence the work reported in this paper.

Data availability

Data cannot be shared as it is part of ongoing study.

Acknowledgements

Maciej Bik has been partly supported by the Foundation for Polish Science (FNP) with the START 2020 scholarship. Maciej Bik was financially supported with a doctoral scholarship from the National Science Centre under the project no. 2020/36/T/ST5/00073. This research project was also supported by the program "Excellence initiative – research university" for the AGH University of Science and Technology. The authors would like to thank Christoph Grimme for his support during preparation of cross-sections, Dr. Gerald Schmidt and Melanie Thalheimer for their support with EPMA analysis and SEM imaging, Aleksander Gil for fruitful discussions, and Mathias Röhrig for his help in setting up the exposure rigs.

Appendix A. Supplementary material

Supplementary data to this article can be found online at https://doi.org/10.1016/j.apsusc.2023.157601.

References

[1] B.P. Bewlay, M. Weimer, T. Kelly, A. Suzuki, P.R. Subramanian, The Science, Technology, and Implementation of TiAl Alloys in Commercial Aircraft Engines, Mater. Res. Soc. Symp. Proc. 1 (2013) 49–58, https://doi.org/10.1557/opl.201.
[2] B.P. Bewlay, S. Nag, A. Suzuki, M.J. Weimer, TiAl alloys in commercial aircraft engines, Mater. High Temp. 33 (2016) 549–559, https://doi.org/10.1080/09603409.2016.1183068.
[3] J. Dai, J. Zhu, C. Chen, F. Weng, High temperature oxidation behavior and research status of modifications on improving high temperature oxidation resistance of titanium alloys and titanium aluminides: A review, J. Alloys Compd. 685 (2016) 784–798, https://doi.org/10.1016/j.jallcom.2016.06.212.
[4] A. Knaislov, P. Nov, M. Cabibbo, L. Jaworska, Development of TiAl – Si Alloys — A Review, Materials (Basel). 14 (2021) 1–22.
[5] F. Appel, H. Clemens, F.D. Fischer, Modeling concepts for intermetallic titanium aluminides, Prog. Mater. Sci. 81 (2016) 55–124, https://doi.org/10.1016/j.pmatsci.2016.01.001.
[6] A. Donchev, M. Schütze, A. Kolitsch, R. Yankov, Optimization of the fluorine effect for improving the oxidation resistance of TiAl-alloys, Mater. Sci. Forum. 706–709 (2012) 1061–1065, https://doi.org/10.4028/www.scientific.net/MSF.706-709.1061.
[7] A. Donchev, L. Mengis, A. Couret, S. Mayer, H. Clemens, M. Galetz, Effects of tungsten alloying and fluorination on the oxidation behavior of intermetallic titanium aluminides for aerospace applications, Intermetallics. 139 (2021), 107270. 10.1016/j.intermet.2021.107270.
[8] J. Wang, L. Kong, J. Wu, T. Li, T. Xiong, Microstructure evolution and oxidation resistance of silicon-aluminizing coating on γ-TiAl alloy, Appl. Surf. Sci. 356 (2015) 827–836. 10.1016/j.apsusc.2015.08.204.
[9] R. Swadźba, L. Swadźba, B. Mendala, P.-P. Bauer, N. Laska, U. Schulz, Microstructure and cyclic oxidation resistance of Si-aluminide coatings on γ-TiAl at 850 °C, Surf. Coatings Technol. 403 (2020), 126361. 10.1016/j.surfcoat.2020.126361.
[10] G. Moskal, D. Migas, B. Mendala, P. Kałamarz, M. Mikuśkiewicz, A. Iqbal, S. Jucha, M. Góral, The Si influence on the microstructure and oxidation resistance of Ti-Al slurry coatings on Ti-48Al-2Cr-2Nb alloy, Mater. Res. Bull. 141 (2021), 111336. 10.1016/j.materresbull.2021.111336.
[11] R. Pflumm, S. Friedle, M. Schütze, Oxidation protection of γ-TiAl-based alloys - A review, Intermetallics. 56 (2015) 1–14, https://doi.org/10.1016/j.intermet.2014.08.002.
[12] L. Mengis, A.S. Ulrich, P. Watermeyer, C.H. Liebscher, M.C. Galetz, Oxidation behaviour and related microstructural changes of two β0–phase containing TiAl alloys between 600 °C and 900 °C, Corros. Sci. 178 (2021), 109085. 10.1016/j.corsci.2020.109085.
[13] L. Mengis, C. Oskay, A. Donchev, M.C. Galetz, Critical assessment of the cyclic oxidation resistance of the aluminized Ti-48Al-2Cr-2Nb TiAl alloy at 700 °C and its impact on mechanical properties, Surf. Coatings Technol. 406 (2021), 126646. 10.1016/j.surfcoat.2020.126646.
[14] Z. Cai, Q. Guo, M. Jiang, X. Jiang, S. Chen, H. Sun, Influence of water vapour on the oxidation behaviour of TiAl based multielement alloys, Intermetallics. 135 (2021), 107229, https://doi.org/10.1016/j.intermet.2021.107229.
[15] T. Dudziak, E. Rząd, J. Morgiel, M. Wytrwal-Sarna, A. Kirchner, M. Pomorska, L. Boron, T. Polczyk, G. Moskal, D. Toboła, B. Klöden, T. Weißgärber, Scale mass gain, morphology and phase composition of air and steam oxidized electron beam melted and cast Ti–48Al–2Nb-0.7Cr-0.3Si alloys, Intermetallics. 145 (2022), https://doi.org/10.1016/j.intermet.2022.107553.
[16] Q. Wen, Z. Yu, R. Riedel, The fate and role of in situ formed carbon in polymer-derived ceramics, Prog. Mater. Sci. 109 (2019), 100623, https://doi.org/10.1016/j.pmatsci.2019.100623.
[17] G. Barroso, Q. Li, R.K. Bordia, G. Motz, Polymeric and ceramic silicon-based coatings-a review, J. Mater. Chem. A. 7 (2019) 1936–1963, https://doi.org/10.1039/c8ta09054h.

[18] A.S. Ulrich, T. Kaiser, E. Ionescu, R. Riedel, M.C. Galetz, Reactive Element Effect Applied by Alloying and SiHfBCN Coating on the Oxidation of Pure Chromium, Oxid. Met. 92 (2019) 281–302, https://doi.org/10.1007/s11085-019-09926-w.
[19] M. Parchovianský, I. Parchovianská, P. Švančárek, D. Medveď, M. Lenz-leite, G. Motz, D. Galusek, High-Temperature Oxidation Resistance of PDC Coatings in Synthetic Air and Water Vapor Atmospheres, (2021).
[20] C. Wu, X. Pan, F. Lin, G. Chen, L. Xu, Y. Zeng, Y. He, D. Sun, High-Temperature Anti-Oxidative Composite Coating Fabricated by Direct Writing, (2022).
[21] P. Jeleń, M. Bik, M. Nocuń, M. Gawęda, E. Długoń, M. Sitarz, Free carbon phase in SiOC glasses derived from ladder-like silsesquioxanes, J. Mol. Struct. 1126 (2016) 172–176, https://doi.org/10.1016/j.molstruc.2016.03.096.
[22] C. Stabler, E. Ionescu, M. Graczyk-Zajac, I. Gonzalo-Juan, R. Riedel, Silicon oxycarbide glasses and glass-ceramics: "All-Rounder" materials for advanced structural and functional applications, J. Am. Ceram. Soc. 101 (2018) 4817–4856, https://doi.org/10.1111/jace.15932.
[23] M. Bik, M. Stygar, P. Jeleń, J. Dąbrowa, M. Leśniak, T. Brylewski, M. Sitarz, Protective-conducting coatings based on black glasses (SiOC) for application in Solid Oxide Fuel Cells, Int. J. Hydrogen Energy. 42 (2017) 27298–27307, https://doi.org/10.1016/j.ijhydene.2017.09.069.
[24] M. Bik, A. Gil, M. Stygar, J. Dąbrowa, P. Jeleń, E. Długoń, M. Leśniak, M. Sitarz, Studies on the oxidation resistance of SiOC glasses coated TiAl alloy, Intermetallics. 105 (2019) 29–38, https://doi.org/10.1016/j.intermet.2018.09.014.
[25] A. Rahmel, M. Schütze, W.J. Quadakkers, Fundamentals of TiAl oxidation – A critical review, Mater. Corros. 46 (1995) 271–285, https://doi.org/10.1002/maco.19950460503.
[26] M. Bik, J. Szewczyk, P. Jeleń, E. Długoń, W. Simka, M. Sowa, J. Tyczkowski, J. Balcerzak, E. Bik, K. Mroczka, M. Leśniak, M. Barańska, M. Sitarz, Optimization of the formation of coatings based on SiAlOC glasses via structural, microstructural and electrochemical studies, Electrochim. Acta. 309 (2019) 44–56, https://doi.org/10.1016/j.electacta.2019.04.080.
[27] M. Bik, M. Galetz, J. Dąbrowa, K. Mroczka, P. Zając, A. Gil, P. Jeleń, M. Gawęda, M. Owińska, M. Stygar, M. Zajusz, J. Wyrwa, M. Sitarz, Polymer Derived Ceramics based on SiAlOC glasses as novel protective coatings for ferritic steel, Appl. Surf. Sci. 576 (2022), 151826, https://doi.org/10.1016/j.apsusc.2021.151826.
[28] C. Xu, M. Zhu, H. Guan, C. Gao, X. Jin, J. Du, Improvement of steam oxidation resistance of the γ -TiAl alloy with microarc oxidation coatings at 900–1200 ℃, Corros. Sci. 209 (2022), 110711 https://doi.org/10.1016/j.corsci.2022.110711.
[29] A. Shaaban, S. Hayashi, M. Takeyama, Effects of water vapor and nitrogen on oxidation of TNM alloy at 650 °C, Corros. Sci. 158 (2019), 108080, https://doi.org/10.1016/j.corsci.2019.07.006.
[30] M. Burtscher, T. Klein, J. Lindemann, O. Lehmann, H. Fellmann, V. Güther, H. Clemens, S. Mayer, An advanced tial alloy for high-performance racing applications, Materials (Basel). 13 (2020) 1–14, https://doi.org/10.3390/ma13214720.
[31] C. Xu, M. Zhu, C. Gao, H. Guan, X. Wang, X. Jin, J. Du, W. Xue, Microstructural characterizations of γ-TiAl alloy after high-temperature steam oxidations at 900, 1000, 1100 and 1200 °C, Mater. Charact. 189 (2022), https://doi.org/10.1016/j.matchar.2022.111979.
[32] J.Y. Park, I.H. Kim, Y. Il Jung, H.G. Kim, D.J. Park, B.K. Choi, High temperature steam oxidation of Al3Ti-based alloys for the oxidation-resistant surface layer on Zr fuel claddings, J. Nucl. Mater. 437 (2013) 75–80, https://doi.org/10.1016/j.jnucmat.2013.01.338.
[33] B.A. Pint, J.A. Haynes, B.L. Armstrong, Performance of advanced turbocharger alloys and coatings at 850–950°C in air with water vapor, Surf. Coatings Technol. 215 (2013) 90–95, https://doi.org/10.1016/j.surfcoat.2012.08.099.
[34] A. Zeller, F. Dettenwanger, M. Schütze, Influence of water vapour on the oxidation behaviour of titanium aluminides, Intermetallics. 10 (2002) 59–72. 10.1016/S0966-9795(01)00104-2.
[35] B. Öztürk, L. Mengis, D. Dickes, U. Glatzel, M.C. Galetz, Influence of Water Vapor and Temperature on the Oxide Scale Growth and Alpha - Case Formation in Ti - 6Al - 4V Alloy, Oxid. Met. 97 (2022) 241–260, https://doi.org/10.1007/s11085-021-10088-x.
[36] M. Bik, P. Jeleń, E. Długoń, E. Bik, K. Mroczka, M. Barańska, M. Sitarz, SiAlOC glasses derived from sol-gel synthesized ladder-like silsesquioxanes, Ceram. Int. 45 (2019) 1683–1690, https://doi.org/10.1016/j.ceramint.2018.10.047.
[37] A.C. Ferrari, J. Roberston, Interpretation of Raman spectra of disordered and amorphous carbon, Phys. Rev. B - Condens. Matter Mater. Phys. 61 (2000) 14095, https://doi.org/10.1007/BF02543692.
[38] A. Mortensen, D.H. Christensen, O. Faurskov Nielsen, E. Pedersen, Raman Spectra of Amorphous A1203 and Al2O3/MoO3 Obtained by Visible and Infrared Excitation, J. Raman Spectrosc. 22 (1991) 47–49, https://doi.org/10.1021/ac60025a004.
[39] C. Boulesteix, V. Kolarik, F. Pedraza, Steam oxidation of aluminide coatings under high pressure and for long exposures, Corros. Sci. 144 (2018) 328–338, https://doi.org/10.1016/j.corsci.2018.08.053.
[40] M. Sowa, A. Olesiński, B. Szumski, A. Maciej, M. Bik, P. Jeleń, M. Sitarz, W. Simka, Electrochemical characterization of anti-corrosion coatings formed on 6061 aluminum alloy by plasma electrolytic oxidation in the corrosion inhibitor-enriched aqueous solutions, Electrochim. Acta. 424 (2022), 140652, https://doi.org/10.1016/j.electacta.2022.140652.
[41] S. Challagulla, K. Tarafder, R. Ganesan, S. Roy, Structure sensitive photocatalytic reduction of nitroarenes over TiO2, Sci. Rep. 7 (2017) 1–11, https://doi.org/10.1038/s41598-017-08599-2.
[42] A. Biedunkiewicz, K. Jach, A. Obrosov, D. Garbiec, M. Bik, M. Sitarz, Z. Kucia, S. Wei, International Journal of Refractory Metals and Hard Materials Ti-Mo- x TiC composites manufactured by U-FAST reactive sintering, 108 (2022). https://doi.org/10.1016/j.ijrmhm.2022.105960.
[43] N. Zheng, W. Fischer, H. Grübmeier, V. Shemet, W.J. Quadakkers, The significance of sub-surface depletion layer composition for the oxidation behaviour of γ-titanium aluminides, Scr. Metall. Mater. 33 (1995) 47–53, https://doi.org/10.1016/0956-716X(95)00155-O.
[44] D. Cao, W. Cai, W. Tao, S. Zhang, D. Wang, D. Huang, Lactic Acid Production from Glucose Over a Novel Nb2O5 Nanorod Catalyst, Catal. Letters. 147 (2017) 926–933, https://doi.org/10.1007/s10562-017-1988-6.
[45] X. Qu, Y. Liu, B. Li, B. Xing, G. Huang, H. Zhao, Z. Jiang, C. Zhang, S.W. Hong, Y. Cao, Nanostructured T-Nb2O5-based composite with reduced graphene oxide for improved performance lithium-ion battery anode, J. Mater. Sci. 55 (2020) 13062–13074, https://doi.org/10.1007/s10853-020-04910-1.
[46] R.A.P. Ribeiro, E. Longo, J. Andrés, S.R. De Lazaro, A DFT investigation of the role of oxygen vacancies on the structural, electronic and magnetic properties of ATiO3 (A = Mn, Fe, Ni) multiferroic materials, Phys. Chem. Chem. Phys. 20 (2018) 28382–28392, https://doi.org/10.1039/c8cp04443k.
[47] H.C. Barshilia, K.S. Rajam, A Raman-scattering study on the interface structure of nanolayered TiAlNTiN and TiNNbN multilayer thin films grown by reactive dc magnetron sputtering, J. Appl. Phys. 98 (2005), https://doi.org/10.1063/1.1946193.
[48] S. Das, S. Guha, R. Ghadai, D. Kumar, B.P. Swain, Structural and mechanical properties of CVD deposited titanium aluminium nitride (TiAlN) thin films, Appl. Phys. A Mater. Sci. Process. 123 (2017) 1–5, https://doi.org/10.1007/s00339-017-1032-0.
[49] M. Yoshihara, K. Miura, Effects of Nb addition on oxidation behavior of TiAl, Intermetallics. 3 (1995) 357–363, https://doi.org/10.1016/0966-9795(95)94254-C.
[50] J.P. Lin, L.L. Zhao, G.Y. Li, L.Q. Zhang, X.P. Song, F. Ye, G.L. Chen, Effect of Nb on oxidation behavior of high Nb containing TiAl alloys, Intermetallics. 19 (2011) 131–136, https://doi.org/10.1016/j.intermet.2010.08.029.
[51] X. Chen, F. Ding, P. Zhang, D. Wei, F. Li, Z. Wang, X. Zhu, G. Ling, Materials at High Temperatures Characterisation and oxidation behaviour of plasma surface alloyed on γ -TiAl alloy, Mater. High Temp. 38 (2021) 83–94, https://doi.org/10.1080/09603409.2020.1859309.
[52] T. Dudziak, P. Datta, H. Du, I.M. Ross, High temperature air oxidation resistance of TiAlCr-Y coated Ti45Al8Nb between 750°C-950°C, Cent. Eur. J. Eng. 3 (2013) 722–731, https://doi.org/10.2478/s13531-013-0132-7.
[53] V. Simova, S. Knittel, M. Cavarroc, L. Martinu, J.E. Klemberg-Sapieha, Amorphous Si–B–C–N coatings for high-temperature oxidation protection of the γ-TiAl alloy, Surf. Coatings Technol. 442 (2022), https://doi.org/10.1016/j.surfcoat.2022.128544.
[54] D.B. Lee, Effect of Cr, Nb, Mn, V, W and Si on high temperature oxidation of TiAl alloys, Met. Mater. Int. 11 (2005) 141–147, https://doi.org/10.1007/BF03027458.
[55] M.A. Henderson, The interaction of water with solid surfaces: Fundamental aspects, Surf. Sci. Rep. 46 (2002) 1–308, https://doi.org/10.1016/0167-5729(87)90001-X.